Greigite as an indicator for salinity and sedimentation rate change: Evidence from the Yangtze River delta, China

Yinglu Chen[1], Weiguo Zhang[1*], Xiaomei Nian[1], Qianli Sun[1], Can Ge[2], Simon M. Hutchinson[3], Qinzi Cheng[1], Feng Wang[4], Jin Chen[1], and Xuanqi Zhao[1]

[1] State Key Laboratory of Estuarine and Coastal Research, East China Normal University, Shanghai, China

[2] Zhejiang Institute of Hydraulics and Estuary, Hangzhou, China

[3] School of Science, Engineering and Environment, University of Salford, Gt. Manchester, M5 4WT, UK

[4] Institute of Marine Sciences, Guangdong Provincial Key Laboratory of Marine Biotechnology, Shantou University, Shantou, China

Correspondence to: W. Zhang, wgzhang@sklec.ecnu.edu.cn

Key points:

- We identify greigite at the boundary of sedimentary facies with marked salinity change in the Yangtze River delta.
- Greigite-bearing layers occurs predominantly in accreting tidal flat facies with a higher sedimentation rate.
- Magnetic identification of greigite can assist stratigraphic differentiation in delta deposits.

This article has been accepted for publication and undergone full peer review but has not been through the copyediting, typesetting, pagination and proofreading process, which may lead to differences between this version and the Version of Record. Please cite this article as doi: 10.1029/2020JB021085.

Abstract

Ferrimagnetic greigite (Fe_3S_4) is widespread in the sedimentary environment. Despite abundant reports of greigite occurrence in marine and lacustrine deposits, its formation mechanisms in deltaic deposits remain poorly studied. Here we investigate greigite in Holocene Yangtze River delta deposits using granulometric, magnetic and geochemical methods. The studied cores consist of tidal river, estuary, shallow marine and delta facies in ascending order. The greigite-bearing layers are found predominantly in the accreting tidal flat facies during the transgression stage and secondarily in the shallow marine facies during the regression stage of the delta's Holocene development. These sedimentary intervals have a higher total sulfur (TS) content and total sulfur to total organic carbon ratios (TS/TOC) suggesting the accumulation of iron sulfides, including greigite, under reducing estuarine and shallow marine conditions. The greigite-bearing layers in the tidal flat facies have lower Sr/Ba ratios, in comparison to the shallow marine facies, indicating a lower salinity environment. Supported by the dating results, it is suggested that the higher sedimentation rate of the tidal flat facies, caused by rapid sea-level rise during the early Holocene, favors the formation and preservation of greigite. Our results indicate that the magnetic detection of greigite provides a simple and useful tool for inferring salinity and sedimentation rate changes, and hence better a understanding of the heterogeneity of depositional processes in Holocene delta environments.

Plain Language Summary

Greigite (Fe_3S_4), an early or late diagenetic magnetic mineral, is an iron sulfide commonly produced during the carbon-iron-sulfur (C-Fe-S) cycle in aquatic environments. Its occurrence is generally found to be linked to water salinity change, which can be used to infer changes in past environmental conditions such as drought and flood events. So far, studies on greigite have focused on marine and lacustrine deposits. Its formation mechanisms in delta environments remain poorly known, where fresh and marine water mixing results in intensive spatial and temporal salinity change. In this study, environmental magnetic measurement and salinity indictors e.g., the ratio of Strontium to Barium (Sr/Ba), the ratio of total Sulfur to total organic carbon (TS/TOC) and total sulfur concentration (TS) are combined to reveal greigite occurrence and its formation conditions**.** Our results show that higher sedimentation rates and marked salinity change associated with rapid sea level rise in the early Holocene is favorable for greigite generation and preservation. We find that magnetic detection of greigite can provide valuable information regarding spatial/temporal variabilities in fresh-marine water mixing and depositional processes in deltaic environment.

Keywords: greigite; environmental magnetism; salinity change; sedimentation rate; stratigraphy correlation; delta environments; Holocene

1. Introduction

Ferrimagnetic greigite (Fe_3S_4) is commonly regarded as a precursor to pyrite (FeS_2), or a product of pyrite oxidation, in sedimentary environments (Cornwell & Morse, 1987; Wilkin & Barnes, 1996; Roberts et al., 2011). Due to its distinct magnetic properties, it has been widely found in lacustrine (Snowball & Thompson, 1988; Reynolds et al., 1999; Tudryn et al., 2010; Fu et al., 2015; Qiang et al., 2018; Li et al., 2019) and marine deposits (Oda & Torii, 2004; Fu et al., 2008; Blanchet et al., 2009; Chang et al., 2014; Liu et al., 2017; Liu et al., 2018; Duan et al., 2020) using magnetic measurement techniques. It is generally agreed that reaction between carbon (C), sulfur (S) and iron (Fe) drives the formation of greigite and pyrite, and a surplus of reactive iron oxides to H_2S favors the occurrence of greigite (Roberts, 2015). C-S-Fe geochemistry reflects interactions between multiple factors such as organic matter content/lability, sedimentation rate and salinity (Fu et al., 2008; Chang et al., 2014; Liu et al., 2017), which are modulated by environmental processes such as climate and sea-level change (Reynolds et al., 1999; Blanchet et al., 2009; Chang et al., 2014; Wang et al., 2014; Liu et al., 2017; Qiang et al., 2018; Li et al., 2019). For example, flood events in Holocene stratigraphy have been offered as an explanation for greigite occurrence in the Santa Barbara Basin, USA, as more terrigenous sediments, versus limited organic carbon input during flood events, favors the dominance of iron oxide over H_2S (Blanchet et al., 2009). In the mid Miocene Paratethys Sea of central Europe, the occurrence of greigite is interpreted as the result of salinity change associated with sea-level variations, with fresher conditions limiting sulfate supply and H_2S production (Liu et al., 2017).

Modern deltas are the product of land and ocean interaction since the Last Glacial Maximum. To the best of our knowledge, the occurrence of greigite has been reported in only a few modern delta deposits in China (Dong, 2014; Wang et al., 2014; Chen et al., 2015; Bai et al., 2016). Such occurrence is often found at the boundaries of sedimentary facies. For example, in the Yellow River delta greigite is found at the two ends of fluvial facies, underlain and overlain by shallow marine and salt marsh facies, respectively (Wang et al., 2014). In core NT from the Yangtze River delta, a greigite layer is found at the top part of the prodelta facies (Bai et al., 2016). Considering the boundary of sedimentary facies represents a marked change in depositional conditions, e.g., from a terrestrially to marine dominated environment, or vice versa, it is inferred that salinity change plays an important role in greigite occurrence (Wang et al., 2014). However, there is no direct evidence for such salinity change to support this hypothesis.

Several geochemical proxies have been proposed to indicate paleosalinity including total sulfur (TS), the ratio of TS to total organic carbon (TOC) and Sr/Ba (Berner & Raisewell, 1984; Wei & Algeo, 2020). In marine environments, abundant sulfate enables reduced sulfide accumulation in sediments resulting in higher TS and TS/TOC values in comparison to freshwater environments (Berner & Raisewell, 1984). In comparison to Ba, Sr is more abundant in the marine environment and therefore a higher Sr/Ba ratio generally indicates greater salinity (e.g., Chen et al., 1997; Wei & Algeo, 2019; Wang et al., 2021). In this study, we report the granulometric, environmental magnetic and geochemical (TOC, TS, Sr/Ba) analyses of three cores from the Yangtze River delta. The objectives of this study are to (i) identify greigite occurrence and characterize the depositional processes responsible for its formation and preservation; (ii) discuss the potential of greigite occurrence as an indicator for salinity and sedimentation rate changes in Holocene delta stratigraphy.

2. Study area and methods

2.1 Study area

The Yangtze River was incised to a maximum depth of 70-80 m in the delta region during the Last Glacial Maximum (Li et al., 2000). Subsequently, deposits have accumulated in the incised valley as a result of post-glacial sea-level rise and the coastline began to migrate landward until maximum transgression around ca. 8 ka (Song et al., 2013). Thereafter, modern deltaic deposits began to prograde with the deceleration of sea-level rise (Li et al., 2000; Song et al., 2013). Therefore, the sedimentary sequence in the paleo-incised valley comprises fluvial facies, estuarine (including distributary-channel, tidal flat and estuary front sub-environments), shallow marine facies and delta facies (including prodelta, delta front and delta plain sub-environments) with shallowing depth (Hori et al., 2002; Lin et al., 2015).

Two cores from Chongming Island (core CM01, 61.8 m, N31°38′28.6″, E121°22′58.5″; core CM02, 58.2 m, N31°32′30.5″, E121°48′56.1″) and one core from Hengsha Island (core HSD, 58.4 m, N31°18′09″, E121°50′50″), located within the paleo-incised valley, were collected for this study with a core recovery of >90% (Figure 1).

When the cores were split under subdued light, one half was kept for optical simulated luminance (OSL) dating. The other half was photographed and the lithology was described. After description, the cores were subsampled at an interval of 5 cm. Shells were picked for AMS-^{14}C measurement by Beta Analytic (Florida, USA). The ages were calibrated using the Calib 8.1 program with the MARINE 20 data set and reported with a two-standard deviation (2σ) uncertainty (Stuiver et al., 2020). A regional marine reservoir effect (ΔR) =0 was applied to the shell samples as the local reservoir age is uncertain (Hori & Satio, 2017). Furthermore, selected samples were subjected to OSL dating in the TL/OSL dating laboratory of East China

Normal University following the method described in Nian et al. (2018a, 2018b). The dating results are summarized in Table 1 and Table 2. The OSL ages were converted to ka BP relative to AD 1950 for comparison to the ^{14}C ages.

On the basis of stratigraphic correlation between cores CM97 and CX03 from adjacent sites (Figure 2), we ascribe the cores to the following sedimentary facies in ascending order: Unit D, tidal river facies; Unit C, estuarine facies; Unit B, shallow marine/prodelta facies and Unit A, delta front and plain facies (Li et al., 2010; Lin et al., 2015; Hori et., 2002; Su et al., 2020). The 8 ka isochron enables each core to be divided into a lower transgressive (Unit D and C) and an upper regressive part (Unit B and A). Unit D forms the bottom part of each core and is characterized by gray or dark gray fine to very fine sand with interbedded thin clayey silt in cores CM01 and CM02, and silt in core HSD. Unit C is characterized by gray or dark gray interbedded sand and clayey silt, which shows an upward-fining trend in CM01 and CM02. Peat layers (5-10 cm in thickness) are found at core depths ca. 41.5 m in CM01, 39.1 m and 43.7 m in CM02, and 39.7 m in HSD, respectively. Unit B is dominated by gray clayey silts, with centimeter thick silt or sand banding and thin shell fragments locally. Unit A comprises the uppermost part of the cores and is composed mainly of gray silt to fine sand. The top layer (ca. 1-2 m in thickness) is composed of yellowish-brown clayey silts with redoximorphic features.

2.2 Methods

Particle-size analysis was conducted at 50 cm intervals using a Coulter LS 13320 laser analyzer. Prior to analysis, the samples were treated with H_2O_2 (30%) and HCl (10%) to remove organic matter and carbonates, respectively.

Bulk magnetic properties were also measured at 50 cm intervals. Magnetic susceptibility was measured using a Bartington Instruments Ltd. MS2 magnetic susceptibility meter and B sensor. Isothermal remanent magnetization (IRM) was imparted in a forward field of 1T and one reversed field (-300 mT) sequentially using an MMPM10 pulse magnetizer. After each magnetization step, the remanence was measured with an AGICO Dual Speed Spinner Magnetometer (JR6). The IRM imparted with a 1T field is referred to as a "saturation" IRM (SIRM). The S ratios (S_{-300}) is calculated as $S_{-300}=100\times(SIRM-IRM_{300mT})/(2\times SIRM)$ (Bloemendal & Liu, 2005).

Selected samples were then subjected to magnetic hysteresis and thermomagnetic analysis using a variable field translational balance (VFTB). Thermomagnetic analysis was measured in a field of 36 mT. A First-order reversal curve (FORC) was measured using a Vibrating Sample Magnetometer (VSM, Lakeshore 8600). The maximum applied field is 500 mT with field increments up to 1.43 mT resulting in a total of 140 FORCs. FORC diagrams were calculated using FORCinel software v3.06 (Harrison & Feinberg, 2008). These samples are processed with the VARIFORC smoothing parameters $S_{c,0}=8$, $S_{c,1}=10$, $S_{b,0}=7$, $S_{b,1}=10$, and $\lambda_c=\lambda_b=0.1$ (Egli, 2013).

Based on the magnetic measurements, 9 samples were subjected to extracted magnetic minerals examination using a JSM-6700F Scanning Electron Microscope (SEM) with Energy Dispersive X-ray Spectroscopy (EDX). Magnetic particles were extracted from bulk sediments by adapting the methods of Petersen et al. (1986). The samples were dispersed in pure water and a rare earth magnet (wrapped in a plastic film) was dipped into the suspension of samples. The particles which attached to the magnet were then washed into an evaporating dish and dried in low temperature. X-ray diffraction (XRD) analysis was performed on the extracted magnetic components using a Philips PW 1710 diffractometer with Cu Kα radiation.

Total organic carbon (TOC), total sulfur (TS), acetic acid (HAc) extractable Sr and Ba were analyzed at a 5 m interval. TS can indicate the accumulation of iron sulfide in reducing sediments. The ratios of TOC/TS and Sr/Ba have been used as proxies of salinity and increase with increasing salinity (Wei & Algeo, 2020). TOC was analyzed using a potassium-dichromate ($K_2Cr_2O_7$) titration method (Lu, 2000), which has a precision better than 5%. TS was analyzed using Eltra CS800 carbon/sulfur analyzer. The analytical precision is within 0.1%. HAc extractable Sr and Ba analysis followed the method developed by Wang et al. (2021) and were determined by inductively coupled plasma-atomic emission spectrometry (ICP-AES, Thermo iCAP 7400), which has precision better than 10%. The weak acid treatment aims to target only the exchangeable and carbonate-related fractions, which are believed to be produced in the depositional environment and to be related specifically to salinity (Wang et al., 2021).

3. Results

3.1 Particle size

The cores display significant variations in particle size composition with depth (Figure 3). In general, they exhibit an upward coarse-fine-coarse succession. The bottom part (Unit D) in cores CM01 and CM02 is dominated by sand (> 63 μm) with values of mean size ranging from 50 to 113 μm and 28 to 129 μm, respectively. In comparison, Unit D in core HSD is dominated by silt (4~63 μm). Unit C is dominated by silt. There is an upward fining trend in CM01 and CM02 in this layer, and an upward coarsening and then fining trend in core HSD (~40 m depth as the transition). Unit B is the finest layer in each core, among which core HSD is coarser than those of core CM01 and CM02. In Unit A, particle size of cores CM01 and CM02 becomes coarser upward and then finer towards the surface. In contrast, core HSD exhibits a general upward increasing trend in particle size. On average, core CM01 and HSD are coarser than core HSD.

3.2 Evidence of greigite

3.2.1 Bulk magnetic properties

Magnetic parameters for cores CM01, CM02 and HSD are illustrated in Figure 4. Higher SIRM/χ values (e.g., >15 kA m $^{-1}$) and S_{-300} are potential indicators of greigite (Roberts, 1995; Walden et al., 1997). We code the higher SIRM/χ value layers in unit B as B1, B2…, and those in unit C as C1, C2… in a downward sequence. Clearly, higher SIRM/χ layers are abundant in unit C which is followed by Unit B. In core CM01, higher values of SIRM/χ occur in three layers in Unit C, including 52.95-53.95 m (C3), 38.45-39.95 m (C2) and 26.45-28.45 m (C1), and a single layer at 21.95-22.95 m in Unit B (B1). The C1 layer is a composite one with two intervals showing higher SIRM/χ and S_{-300} values. Among the higher SIRM/χ layers in core CM01, C2 has the most pronounced greigite signal. In core CM02, relatively high values of SIRM/χ occur at 35.05-43.55 m (C1) and 19.05-20.05 m (B1), with the former being a composite layer, which contains more sub-layers than that of C1 in CM01. In this core the higher SIRM/χ signal is much stronger in C1 than in B1. In core HSD, higher values of SIRM/χ occur at 55.15-54.75 m (C2) and 34.55-37.65 m (C1), respectively. The C2 and C1 layer are also a composite feature consisting of two layers (Figure 4). Clearly, pronounced higher SIRM/χ layers occur primarily near the lower and upper boundaries of Unit C. On the other hand, those seen in Unit B have a generally lower SIRM/χ value implying that greigite is less dominant here. The C1 layer is occurring at top boundary of unit C and therefore comparable among the cores. The C1 layer in core HSD has highest SIRM/χ values followed by those in cores CM02 and CM01. Other layers are not occurring in all the cores at comparable position in the stratigraphy, e.g., B1 is not present in core HSD, while C2 is only shown in core CM01 and C2/C3 is not present in core CM02.

3.2.2 Thermomagnetic analysis

Thermomagnetic analysis of typical greigite-bearing samples from core CM01 are presented in Figure 5a-d. Magnetization of all the samples shows a gradually increasing trend with increasing temperature until ~270□ and then undergoes an irreversible drop between 270□ and 400□. The samples with the highest SIRM/χ values (Figure 5c) show the most obvious increase when heated to ~270□. This feature is consistent with the thermomagnetic heating curve of greigite in air using a non-saturating field (Dekkers et al., 2000; Roberts et al., 2011). Rather than continuously decreasing, magnetization increases with heating above 440□ and then exhibits a Curie temperature of 570-580□, which is suggestive of the conversion of weakly magnetic paramagnetic minerals (e.g., pyrite) to magnetite (Passier & Dekkers, 2001; Roberts et al., 2011). The samples without clearly greigite signals are shown in Figure 5i-l. The sample with lower TS content (Figure 5i-j) shows a clear Curie temperature of magnetite. The sample with higher TS content (Figure 5k-l) shows an obvious peak around 450°C on the heating curve, suggesting the conversion of pyrite to magnetite during heating process (Passier & Dekkers, 2001).

3.2.3 FORC diagrams and hysteresis properties

Greigite-bearing samples are usually characterized by closed circled contours with a central peak shifted to negative interaction fields in a FORC diagram (Roberts et al., 2011). Our greigite-containing samples show two FORC diagram types. One type (Group I), with higher SIRM/χ values, has one closed concentric contour with a large Bu spread that indicates a SD contribution with significant magnetostatic interactions among magnetic grains (Figure 6a). A second type (Group II), with moderate SIRM/χ values, shows the presence of an additional mineral with a Bc of 20 mT, indicating a mixture of greigite with varying amounts of magnetite (Figure 6b, c, d). It is clear that greigite dominance over magnetite increases with increasing SIRM/χ values (Figure 6). On the Day plot, samples with higher SIRM/χ values fall closer to the SD field (Day et al., 1977) in comparison to samples without greigite signals (Figure 6i).

3.3 SEM and XRD analysis of magnetic extracts

Scanning electron microscopy of extracted magnetic minerals from representative samples with higher SIRM/χ and SIRM are shown in Figure 7. Greigite occurs as grains with sizes less than 1 μm, while euhedral or framboid pyrite grains are larger (Roberts et al., 2011). The Fe to S atomic ratios for greigite grains display values around 0.75, which is consistent with the ratio of greigite (0.75) and higher than that of pyrite (0.5). The result of XRD analyses confirms that the co-existence of pyrite and greigite (Figure 7j).

3.4 TOC, TS and Sr/Ba

Downcore variations in TOC, TS, TOC/TS and Sr/Ba for cores CM01, CM02 and HSD are illustrated in Figure 8. In general, TOC is lower in Units D and A, and higher in Units C and B. TS and TS/TOC are also lower in Units D and A, and lower part of Unit C. They show a rapid increase toward the top part of Unit C and then decline upward in Unit B. The Sr/Ba ratio is generally lower in Unit D and lower part of Unit C, and increases quickly near the top of Unit C. It remains highest value in Unit B on the whole, although several layers of lower values are observed. It then declines towards Unit A.

4. Discussion

4.1 Influence of salinity change

Our results reveal that greigite occurs primarily in Unit C, especially at the upper part of this unit. Such layers correspond to an increasing an TS content and TS/TOC ratio, indicating that greigite occurrence is associated with iron sulfide accumulation under reducing conditions (Figure 8). In samples showing dominance of magnetic properties by magnetite (Figure 5i, j), magnetite is primarily a detrital origin in association with lower TS content of the sample. Under reducing condition, magnetite is reduced to produce iron sulfide, as demonstrated by its mixture with greigite to a varying degree in different sedimentary layers (Figure 6). However, not all layers with a higher TS exhibit greigite occurrence (e.g., Unit B). The higher TS layers, without an obvious greigite signal contain more pyrite as reflected by the hump around 450°C on the thermomagnetic curves (Figure 5k, l) (Passier & Dekkers, 2001), suggesting an advanced degree of pyritization.

Formation of greigite is generally ascribed to insufficient H_2S supply compared to active iron oxides, which retards the formation of pyrite (Roberts et al., 2011). Diminished H_2S availability can be caused by lower levels of labile organic carbon or sulfate. Since our greigite-bearing samples occur primarily in estuary facies (Unit C), which has a higher proportion of terrestrial organic carbon than the overlying shallow marine facies (Pan et al., 2020), organic carbon lability may restrict sulfate reduction and hence favor greigite formation. In the Holocene stratigraphy of the Yangtze River delta, there are significant salinity and sulfate abundance changes associated with freshwater-seawater mixing during marine transgression and delta progradation processes (Figure 8). Our studies indicate that the tidal river (Unit D) has lower Sr/Ba values and therefore a lower salinity. Salinity is variable and relatively low in the lower part of Unit C, but increases towards the boundary of Unit C and B. With a further rise of sea-level, the coring sites became a shallow marine environment. This change in environment led to an abrupt increase of salinity. Salinity peaks in Unit B, although fluctuations in salinity are observable. Foraminifera analysis also indicates that the estuary facies (Unit C) had a weaker marine influence than the overlying shallow marine/prodelta facies (Unit B) (Hua, 1988; Ke et al., 2017). Then, with delta facies (Unit A) prograding into the coring sites, salinity lowers due to the increasing influence of freshwater mixing (Figure 2).

The coincidence of greigite layer C1 with lower salinity, but rising salinity at the upper boundary of unit C therefore indicates that intermediate salinity is likely to be a controlling factor (Snowball & Thompson, 1988). When conditions became saline, due to a rising sea-level in the early Holocene, increasing sulfate concentration favored greigite generation first. When the coring site became a shallow marine environment after ca. 8 ka (i.e., Unit B), salinity became high enough so that sulfate was no longer a limiting factor during the sulfidization process; consequently, pyrite became dominant, as reflected by higher TS contents of Unit B.

The additional greigite layers C3 in CM01 and C2 in HSD correspond to the transition from tidal river to estuary facies with increasing salinity levels. However, in the early stages of the Holocene transgression, salinity was lower in comparison to the overlying sedimentary facies with a lower level of sulfate. Therefore, we see a lower level of iron sulfide accumulation including greigite. The greigite layer is not present in core CM02, which highlights the spatial heterogeneity of sedimentary conditions in delta environments (Cheng et al, 2020).

The greigite layer B1 in Unit B of cores CM01 and CM02 occurs where water conditions became fresher and less saline as reflected by the Sr/Ba values. With such a transition, sulfate becomes lower and possibly limits the generation of greigite and its full transformation into pyrite. The lower TS content around this depth also indicates that limited sulfur accumulation in certain intervals of the shallow marine facies occurred, implying fluctuating salinity conditions. It is of note that greigite is more abundant in core CM01, in comparison to CM02, with the latter having a higher Sr/Ba ratio. No obvious greigite is presented in Unit B of core HSD, which has highest Sr/Ba ratios in comparison to its counterpart in CM01 and CM02. This again suggests that lower salinity favors greigite formation and preservation, which is in accordance with the greater abundance of greigite in Unit C in comparison to Unit B, although the latter has higher salinity as suggested by the Sr/Ba ratios. Overall, greigite occurrence at the boundary of sedimentary facies is consistent with our previous findings in the Yellow River delta (Wang et al., 2014).

4.2 Influence of sedimentation rate

The retarded pyritization we have observed could also be related to the sedimentation rate. The greigite layers in Unit C have an age older than 8-9 ka (Figure 2), when rapid sea-level rise during early Holocene resulted in higher sedimentation rates (Nian et al., 2018a, 2018b). In core CM97, it has been found that core depth 61.06-40.2 m covers a period spanning 12,000 cal. a BP to 9,000 cal. a BP, with a mean sedimentation rate of 10 m/ka (Hori & Saito, 2017). Similarly, Unit C has a sedimentation rate of ca. 17, 11 and 4 m/ka in core CM01, CM02 and HSD, respectively. Due to rapid deposition, sulfate reduction lacks sufficient time for sulfide accumulation, which can favor greigite over pyrite formation (Aben et al., 2014；Figure 9). In core CM97, it has been found that core depth 25.43-20.48 m has an age ranging from 8500 cal. a BP to 1400 cal. a BP, with a mean sedimentation rate of only 1 m/ka (Hori & Saito, 2017). Similarly, Unit B has a mean sedimentation rate of 1.6, 2.3 and 3.0 m/ka in cores CM01, CM02 and HSD respectively. The lower sedimentation rate in this part of the core may allow enough time for sulfide accumulation and the conversion of greigite to pyrite. Accordingly, greigite occurrence is more frequent and more pronounced in Unit C than in Unit B.

4.3 Paleoenvironmental implications

The greigite layer in C1 marks a change toward rising salinity, as well as a higher sedimentation rate, in response to rapid sea-level rise in the early Holocene. The fine-grained particle size composition of the C1 layer (i.e., clayey silt) and the occurrence of peat layers (ca. 39-44 m) is suggested that the C1 layer and C2 layer in core CM01 belong to tidal flat facies, which can be correlated with the accreting flood plain facies (39-56 m depth) occurring in core CX03 (Li et al., 2010) and tidal flat facies occurring around 40 m in core CM97 (Hori et al., 2002) and core CSJA6 (Yu et al., 2016) (Figure 1). We infer that the tidal flat facies accrete upward with rising sea-level until 9 ka, as they show a similar particle size composition (Rahman & Plater, 2014). The C1 layer in core CM01 possibly experienced much fresher water conditions and a stronger terrestrial organic carbon input due to its landward position, resulting in less greigite production and preservation. The multiple greigite peaks in the composite layer (C1) probably reflect fluctuating depositional conditions over a short period i.e., 10-9 ka according to the dating results (Figure 2). The more frequent fluctuations in the thicker C1 layer of core CM02, in comparison to the other two cores, also reflects the spatial variability of depositional processes (Cheng et al., 2020). Integrated with high-resolution dating, magnetic measurements could therefore offer paleoclimatic and environmental variability information on a centennial scale.

Our results show that greigite layer occurrence can be used efficiently for probing salinity changes in Holocene stratigraphy in delta environments and hence stratigraphic division. Traditionally, stratigraphy division is based on sediment structure and the microfossil assemblage (e.g., diatoms, foraminifera). However, neither provide characteristics unique to particular sedimentary facies. Furthermore, the analysis of microfossil is time-consuming and can be problematic in certain environments. In contrast, magnetic, measurements are simple and quick, allowing for high resolution stratigraphic division and paleoenvironmental studies. Considering the heterogeneous nature of delta deposits in space and time, as demonstrated by the three cores in this study and previous studies in the area (Cheng et al., 2020), our approach has wider implications in paleoenvironmental studies using delta deposits.

5. Conclusions

The occurrence of greigite in Holocene Yangtze River delta deposits has been confirmed by magnetic, SEM and XRD analyses. Multiple greigite layers occur in rapidly accreting tidal flat facies with an age older than ca. 8 ka with an individual greigite layer in the overlying shallow marine facies. This distribution suggests that greigite is more abundant in the transgressional, than the regressional deposits of delta stratigraphy in the study area. The former represents the response to a swiftly rising sea-level in the early Holocene with fluctuating salinity conditions. The intermediate salinity and higher sedimentation rates during the marine transgression are favorable for greigite formation and preservation. Greigite depth distribution patterns may enable reliable stratigraphic correlation between the cores; however, core-specific differences exist reflecting the heterogeneity of depositional processes in Holocene stratigraphy in delta environments. Our results demonstrate that the magnetic detection of greigite can provide a simple and quick tool to infer salinity changes, which has implications for reconstructing the history of fluvial-marine interactions in heterogenous delta environments with a higher spatial and temporal resolution.

Acknowledgments

The data presented in this manuscript will be available at https://figshare.com/articles/dataset/dataset/13669739. This work was supported by the grants from the National Natural Science Foundation of China (41976158, 41576094 and 41771009) and the Ministry of Science and Technology of China (2017YFE0107400). We thank Associate Editor Mark J. Dekkers and the anonymous reviewers whose constructive comments improved this manuscript. We also thank Chenyao Yan for her help with experimental analysis.

References

Aben, F. M., Dekkers, M. J., Bakker, R. R., Hinsbergen, D. J. J., Zachariasse, W. J., Tate, G. W., et al. (2014). Untangling inconsistent magnetic polarity records through an integrated rock magnetic analysis: A case study on Neogene sections in East Timor. *Geochemistry, Geophysics, Geosystems*, 15, doi:10.1002/2014GC005294.

Aitken, M. J. (1988). An introduction to optical dating. New York: Oxford University Press.

Arnold, L. J., Bailey, R. M., Tucker, G. E. (2007). Statistical treatment of fluvial dose distributions from southern Colorado arroyo deposits. *Quaternary Geochronology*, *2*(1-4), 162-167.

Bai, X. X., Zhang, W. G., Pan, D. D., Wang, Z. H., Sun, Q. L., Chen, J., et al. (2016). Magnetic properties of Holocene tidal flats in the Yangtze delta and their paleoenvironmental implications (in Chinese). *Acta Sedimentologica Sinica*, *34*(6), 1165-1175.

Berner, R. A., & Raisewell, R. (1984). C/S method for distinguishing freshwater from the marine sedimentary rocks. *Geology*, *12*, 365-368. https://doi.org/10.1130/0091-7613(1984)122.0.CO;2

Blanchet, C. L., Thouveny, N., & Vidal, L. (2009). Formation and preservation of greigite (Fe_3S_4) in sediments from the Santa Barbara Basin: Implications for paleoenvironmental changes during the past 35 ka. *Paleoceanography*, *24*, PA2224. https://doi.org/10.1029/2008PA001719

Bloemendal, J., & Liu, X. M. (2005). Rock magnetism and geochemistry of two plio-pleistocene Chinese loess-palaeosol sequences-implications for quantitative palaeoprecipitation reconstruction. *Paleogeography Paleoclimatology, Paleoecology*, *226*, 149-166. https://doi.org/10.1016/j.palaeo.2005.05.008

Chang, L., Vasiliev, I., Baak, van C., Krijgsman, W., Dekkers, M. J., Roberts, A. P., et al. (2014). Identification and environmental interpretation of diagenetic and biogenic greigite in sediments: A lesson from the Messinian Black Sea. *Geochemistry, Geophysics, Geosystems*, *15*, 3612-3627. https://doi.org/10.1002/2014GC005411

Chen, T., Wang, Z. H., Wu, X. X., Gao, X. Q., Li, L., & Zhan, Q. (2015). Magnetic properties of tidal flat sediments on the Yangtze coast, China: Early diagenetic alteration and implications. *The Holocene*, *25*(5), 832-843. https://doi.org/10.1177/0959683615571425

Chen, Z. Y. & Chen, Z. L. (1997). Quaternary stratigraphy and trace-element indices of the Yangtze delta, eastern China, with special reference to marine transgressions. *Quaternary Research*, *47*, 181-191. https://doi.org/10.1006/qres.1996.1878

Cornwell, J. C. & Morse, J. W. (1987). The characterization of iron sulfide minerals in anoxic marine sediments. *Marine Chemistry*, *22*, 193-206. https://doi.org/10.1016/0304-4203(87)90008-9

Cheng, Q. Z., Wang, F., Chen, J., Ge, C., Chen, Y. L., Zhao, X. Q., et al. (2020). Combined chronological and mineral magnetic approaches to reveal age variations and stratigraphic heterogeneity in the Yangtze River subaqueous delta. *Geomorphology*, *359*, 107163. https://doi.org/10.1016/j.geomorph.2020.107163

Day, R., Fuller, M., & Schmidt, V. A. (1977). Hysteresis properties of titanomagnetites-grain-size and compositional dependence. *Physics of the Earth and Planetary Interiors*, *13*, 260-267. https://doi.org/10.1016/0031-9201(77)90108-X

Dong, Y. (2014). Magnetic properties of Holocene sediments from coastal region in Nantong and their paleoenvironmental implications, (Doctoral dissertation). Retrieved from Deep Blue. (http://202.120.82.200:8800/docinfo.action?id1=a39d154ea3eff18bf9f61cc79d03e165&id2=QQWI27UokPQ%253D). Shanghai: East China Normal University.

Duan, Z. Q., Liu, Q. S., Qin, H. F., Zhao, X. X., & Gao, X. (2020). Behavior of greigite-bearing marine sediments during AF and thermal demagnetization and its significance. *Geochemistry, Geophysics Geosystems*, *21*, e2019GC008635. https: // doi.org/10.1029/2019GC008635

Dekkers, M. J., Passier, H. F., & Schoonen, M. A. A. (2000). Magnetic properties of hydrothermally synthesized greigite (Fe_3S_4)-II. High- and low-temperature characteristics. *Geophysical Journal International*, 141, 809-819. https://doi.org/10.1046/j.1365-246x.2000.00129.x

Egli, R. (2013). VARIFORC: An optimized protocol for calculating non-regular first-order reversal curve (FORC) diagrams. *Global and Planetary Change*, *110*, 302-320. https://doi.org/10.1016/j.gloplacha.2013.08.003

Fu, C. F., Bloemendal, J., Qiang, X. K., Hill, M. J., & An, Z. S. (2015). Occurrence of greigite in the Pliocene sediments of Lake Qinghai, China, and its paleoenvironmental and paleomagnetic implications. *Geochemistry, Geophysics, Geosystems*, *16*, 1293-1306. https://doi.org/10.1002/2014GC005677

Fu, Y. Z., Dobeneck, T. V., Franke, C., Heslop, D., & Kasten, S. (2008). Rock magnetic identification and geochemical process models of greigite formation in Quaternary marine sediments from the Gulf of Mexico (IODP Hole U1319A). *Earth and Planetary Science Letters*, *275*, 233-245. https://doi.org/10.1016/j.epsl.2008.07.034

Galbraith, R. F., Roberts, R. G., Laslett, G. M., Yoshida, H., & Olley, J. M. (1999). Optical dating of single and multiple grains of quartz from Jinmium rock shelter, northern Australia. Part I. *Archaeometry*, *41*, 339-364.

Harrison, R. J. & Feinberg, J. M. (2008). FORCinel: An improved algorithm for calculating first-order reversal curve distributions using locally weighted regression smoothing. *Geochemistry, Geophysics, Geosystems*, *9*, Q5016. https://doi.org/10.1029/2008GC001987

Hori, K., & Saito, Y. (2017). Differences in radiocarbon ages among molluscan shells, plant materials, and total organic carbon: An example from the paleo-Changjiang incised-valley fill, China. *Quaternary International*, *455*, 45-55. https://doi.org/10.1016/j.quaint.2017.07.037

Hori, K., Saito, Y., Zhao, Q. H., & Wang, P. X. (2002). Evolution of the coastal depositional systems of the Changjiang (Yangtze) River in response to late Pleistocene-Holocene sea-level changes. *Journal of Sedimentary Research*, *72*, 884–897. https://doi.org/10.1306/052002720884

Hua, D. (1988). On characteristics of the microfauna of Holocene in the mouth bars of the Changjiang estuary and its significance (in Chinese). *Journal of East China Normal University (Natural Science)*, (1), 88-95.

Ke, X., Li, B. H., Zhang, Z. Y., Wei, L., Hu, F., Fan, D. W., et al. (2017). Post-glacial foraminifera of the incised Yangtze paleo-valley and paleoenvironmental implications. *Journal of Paleontology*, *91*(6), 1102-1122. https://doi.org/10.1017/jpa.2017.66

Li, B. H., Wang Q., & Li, C. X. (2010). Correlation of stratigraphic architecture of sub-deltas of Changjiang River delta (in Chinese). *Journal of Palaeogeography*, *12*(6), 685-698.

Li, C. X., Chen, Q. Q., Zhang, J. Q., Yang, S. Y., & Fan, D. D. (2000). Stratigraphy and paleoenvironmental changes in the Yangtze delta during late Quaternary. *Journal of Asian Earth Science*, *18*, 453-469. https://doi.org/10.1016/S1367-9120(99)00078-4

Li, W., Mu, G. J., Zhang, W. G., Lin, Y. C., Zhang, D. L., & Song, H. Z. (2019). Formation of greigite (Fe_3S_4) in the sediments of saline ake Lop Nur, northwest China, and its implications for paleo-environmental change during the last 8400 years. *Journal of Asian Earth Science*, *174*, 99-108. https://doi.org/10.1016/j.jseaes.2018.11.021

Lin, C. M., Zhang, X., Xu, Z. Y., Deng, C. W., Yin, Y., & Cheng, Q. Q. (2015). Sedimentary characteristics and accumulation conditions of shallow-biogenic gas for the late Quaternary sediments in the Changjiang River delta area (in Chinese). *Advances in Earth Science*, *30*(5), 589-601

Liu, J. X., Mei, X., Shi, X. F., Liu, Q. S., Liu, Y. G., & Ge, S. L. (2018). Formation and preservation of greigite (Fe_3S_4) in a thick sediment layer from the central South Yellow Sea. *Geophysical Journal International*, *213*, 135-146. https://doi.org/10.1093/gji/ggx556

Liu, J., Saito, Y., Kong, X. H., Wang, H., Xiang, L. H., Wen, C., & Nakashima, R. (2010). Sedimentary record of environmental evolution off the Yangtze River estuary, East China Sea, during the last ~13,000 years, with special reference to the influence of the Yellow River on the Yangtze River delta during the last 600 years. *Quaternary Science Reviews*, *29*, 2424-2438. https://doi:10.1016/j.quascirev.2010.06.016

Liu, S. Z., Krijgsman, W., Dekkers, M. J., & Palcu, D. (2017). Early diagenetic greigite as an indicator of paleosalinity changes in the middle Miocene Paratethys Sea of central Europe. *Geochemistry, Geophysics, Geosystems*, *18*, 2634-2645. https://doi.org/10.1002/2017GC006988

Lu, R. K. (2000). Soil and agricultural chemistry analysis method (in Chinese). Beijing: China Agricultural Science and Technology Press.

Nian, X. M, Zhang, W. G., Wang, Z. H., Sun, Q. L., Chen, J., & Chen, Z. Y. (2018a). Optical dating of Holocene sediments from the Yangtze River (Changjiang) delta, China. *Quaternary International*, *467*, 251-263. https://doi.org/10.1016/j.quaint.2018.01.011

Nian, X. M., Zhang, W. G., Wang, Z. H., Sun, Q. L., Chen, J., & Chen, Z. Y. (2018b). The chronology of a sediment core from incised valley of the Yangtze River delta: comparative OSL and AMS ^{14}C dating. *Marine Geology*, *395*, 320-330. https://doi.org/10.1016/j.margeo.2017.11.008

Oda, H., & Torii, M. (2014). Sea-level change and remagnetization of continental shelf sediments off New Jersey (ODP Leg 174 A): Magnetite and greigite diagenesis. *Geophysical Journal International*, *156*, 443-458. http://doi.org/10.1111/j.1365-246X.2004.02162.x

Pan, D. D., Wang, Z. H., Zhan, Q., Saito, Y., Wu, H., Yang, S. Y., et al. (2020). Organic geochemical evidence of past changes in hydro- and sediment-dynamic processes at river mouths: A case study of Holocene sedimentary records in the Changjiang River delta, China. *Continental Shelf Research*, *204*, 104189. https://doi.org/10.1016/j.csr.2020.104189

Petersen, N., von Dobeneck, T., & Vali, H. (1986). Fossil bacterial magnetite in deep-sea sediments from the South Atlantic Ocean. *Nature*, 320, 611-614.

Passier, H. F., de Lange, G. J. & Dekkers, M. J. (2001). Rock-magnetic properties and geochemistry of the active oxidation front and the youngest sapropel in the eastern Mediterranean. *Geophysical Journal International*, 145(3), 604–614. https://doi.org/10.1046/j.0956-540x.2001.01394.x

Qiang, X. K., Xu, X., Zhao, H., & Fu, C. F. (2018). Greigite formed in early Pleistocene lacustrine sediments from the Heqing Basin, southwest China, and its paleoenvironmental implications. *Journal of Asian Earth Sciences*, *156*, 256-264. https://doi.org/10.1016/j.jseaes.2018.01.033

Rahman, R. & Plater, A. J. (2014). Particle-size evidence of estuary evolution: A rapid and diagnostic tool for determining the nature of recent saltmarsh accretion. *Geomorphology*, 139-152. https://doi.org/10.1016/j.geomorph.2014.01.004

Reynolds, R. L., Rosenbaum, J. G., Metre, van P., Tuttle, M., Callender, E., & Goldin, A. (1999). Greigite (Fe_3S_4) as an indicator of drought–the 1912-1994 sediment magnetic record from White Rock Lake, Dallas, Texas. USA. *Journal of Paleolimnology*, *21*(2), 193-206. https://doi.org/10.1023/A:1008027815203

Roberts, A. P. (2015). Magnetic mineral diagenesis. *Earth Science Reviews*, *151*,1-47. https://doi.org/10.1016/j.earscirev.2015.09.010

Roberts, A. P. (1995). Magnetic properties of sedimentary greigite (Fe_3S_4). *Earth and Planetary Science Letters*, *134* (3), 227-236. https://doi.org/ 10.1016/0012-821X (95)00131-U

Roberts, A. P., Chang, L., Rowan, C. J. Horng, C. S., & Florindo, F. (2011). Magnetic properties of sedimentary greigite (Fe_3S_4): An update. *Reviews of Geophysics*, *49*, RG1002. https://doi.org/10.1029/2010RG000336

Snowball, I., & Thompson, R. (1988). The occurrence of greigite in sediments from Loch Lomond. *Journal of Quaternary Science*, *3*, 121-125. https://doi.org/10.1002/jqs.3390030203

Song, B., Li, Z., Saito, Y., Okuno, J., Li, Z., Lu, A. Q., et al. (2013). Initiation of the Changjiang (Yangtze) delta and its response to the mid Holocene sea level change. *Palaeogeography, Palaeoclimatology,* *Palaeoecology*, *388*, 81-97. https://doi.org/10.1016/j.palaeo.2013.07.026

Su, J. F., Fan, D. D., Liu, J. P., & Wu, Y. J. (2020). Anatomy of the transgressive depositional system in a sediment-rich tide-dominated estuary: The paleo-Yangtze estuary, China. *Marine and Petroleum Geology*, *121*, 104588. https://doi.org/10.1016/j.marpetgeo.2020.104588

Stuiver, M., Reimer, P.J., and Reimer, R.W., 2020, CALIB 8.2 [WWW program] at http://calib.org, accessed 2020-9-22.

Tudryn, A., Tucholka, P., Gibert, E., Gasse, F., & Wei, K. (2010). A late Pleistocene and Holocene mineral magnetic record from sediments of Lake Aibi, Dzungarian Basin, NW China. *Journal of Paleolimnology*, *44*(1), 109-121. https://doi.org/10.1007/s10933-009-9391-y

Walden, J., Oldfield, F., & Smith, J. P. (1997). Environmental magnetism: A practical guide. Technical Guide 6. (pp.243). London: Quaternary Research Association.

Wang, A. H., Wang, Z. H., Liu, J. K., Xu, N. C., & Li, H. L. (2021). The Sr/Ba ratio response to salinity in clastic sediments of the Yangtze River Delta. *Chemical Geology, 559*, 119923. https://doi.org/10.1016/j.chemgeo.2020.119923

Wang, Y. H., Zhang, W. G., Liu, X. J., Li, G. X., & Liu, M. (2014). Formation of greigite under different climate conditions in the Yellow River delta (in Chinese). *Science China: Earth Sciences*, *44*(10), 2193-2201. http://doi.org/10.1007/s11430-014-4981-6

Wei, W., & Algeo, T. J. (2020). Elemental proxies for paleosalinity analysis of ancient shales and mudrocks. *Geochimica et Cosmochimi*ca *Acta*, *287*(15): 341-366. https://doi.org/10.1016/j.gca.2019.06.034

Wilkin, R. T. & Barnes, H. L. (1996). Pyrite formation by reactions of iron monosulfides with dissolved inorganic and organic sulfur species. *Geochimica et Cosmochimica Acta*, *60*(21), 4167-4179. https://doi.org/10.1016/S0016-7037(97)81466-4

Yu, J. J., Hu, F., Yang, Z. L., Zhang, Z. Y., Jiang, R., Ke, X., et al. (2014). Identification of Holocene foraminifera assemblages in Sijia town of Nantong city, Jiangsu province, and its geological significance (in Chinese). *Geological Bulletin of China*, *30*(10), 1690-1620.

Figure captions

Figure 1. (a) Location of the study area in China. (b) Locations of the cores in the study area e.g., CM01, CM02 and HSD (red dots) along with CM97 (Hori et al, 2002), CX03 (Li et al., 2010; Su et al., 2020), CSJA6 (Yu et al., 2014) and ECS0702 (Liu et al., 2010) from previous studies (blue dots). The red dashed line marks the boundary of paleo-incised valley (Li et al., 2000). (c) Stratigraphic architecture across the Yangtze Delta (modified after Li et al., 2000, Hori et al., 2002, Wang et al., 2018).

Figure 2. Lithology of cores CM01, CM02 and HSD and stratigraphic correlation between neighboring cores CM97 (Hori et al., 2002; Hori & Satio, 2017), CX03 (Li et al., 2010; Su et al., 2020; the fluvial facies at the bottom of the core is not shown). Each core is composed of tidal river (Unit D), estuary (Unit C), shallow marine/prodelta (Unit B) and delta plain and front (Unit A) facies in ascending order.

Figure 3. Downcore variations in particle size composition and mean size in cores CM01, CM02 and HSD. The dashed line marks the boundary between the sedimentary facies (Unit A-D) as defined in Figure 2.

Figure 4. Downcore variations of magnetic properties in cores CM01, CM02 and HSD. The green color bands depict the greigite-bearing layers in Unit B (B1) and Unit C (C1-C3). The dashed lines mark the boundary between the sedimentary facies (Unit A-D) as defined in Figure 2.

Figure 5. Representative thermomagnetic curves for samples from greigite-bearing layers C3-C1 and B1 (see Figure 4) in core CM01(a, c, e, g) and samples without clear greigite signal in core HSD (i, k). The red and blue lines show the heating and cooling process, respectively. The plot showing only the heating curve (b, d, f, h, j, l) corresponds to the respective left panel showing completer heating-cooling cycle curves.

Figure 6. (a-d) First-order reversal curve (FORC) diagrams for typical samples in core CM01 and their positions on the Day plot (e). FORC diagrams in (a) indicate a significant SD greigite contribution (Group I), while (b-d) indicate a mixture of magnetite with greigite (Group II). These samples are processed with the VARIFORC smoothing parameters $S_{c,0}$=8, $S_{c,1}$=10, $S_{b,0}$=7, $S_{b,1}$=10, and $\lambda_c=\lambda_b$=0.1 (Egli, 2013). The Day plot show samples from cores CM01 (bule circles), CM02 (green circles) and HSD (red circles).

Figure 7. (a-c) SEM images and corresponding EDX spectra of magnetic extracts for greigite-bearing samples from cores CM01 (a-c), CM02 (d-f) and HSD (g-i), respectively. (j) Typical XRD results confirm the presence of greigite and pyrite.

Figure 8. Downcore variations of total organic carbon (TOC), total sulfur (TS), TS/TOC, Sr/Ba and first-order derivative of Sr/Ba for core CM01, CM02 and HSD, respectively. The green color bands depict the greigite-bearing layers. The dashed line marks the boundary between the sedimentary facies (Unit A-D) as defined in Figure 2.

Figure 9 A schematic diagram showing effects of sedimentation rate and salinity on the formation of greigite and pyrite in Holocene stratigraphy of the Yangtze River delta.

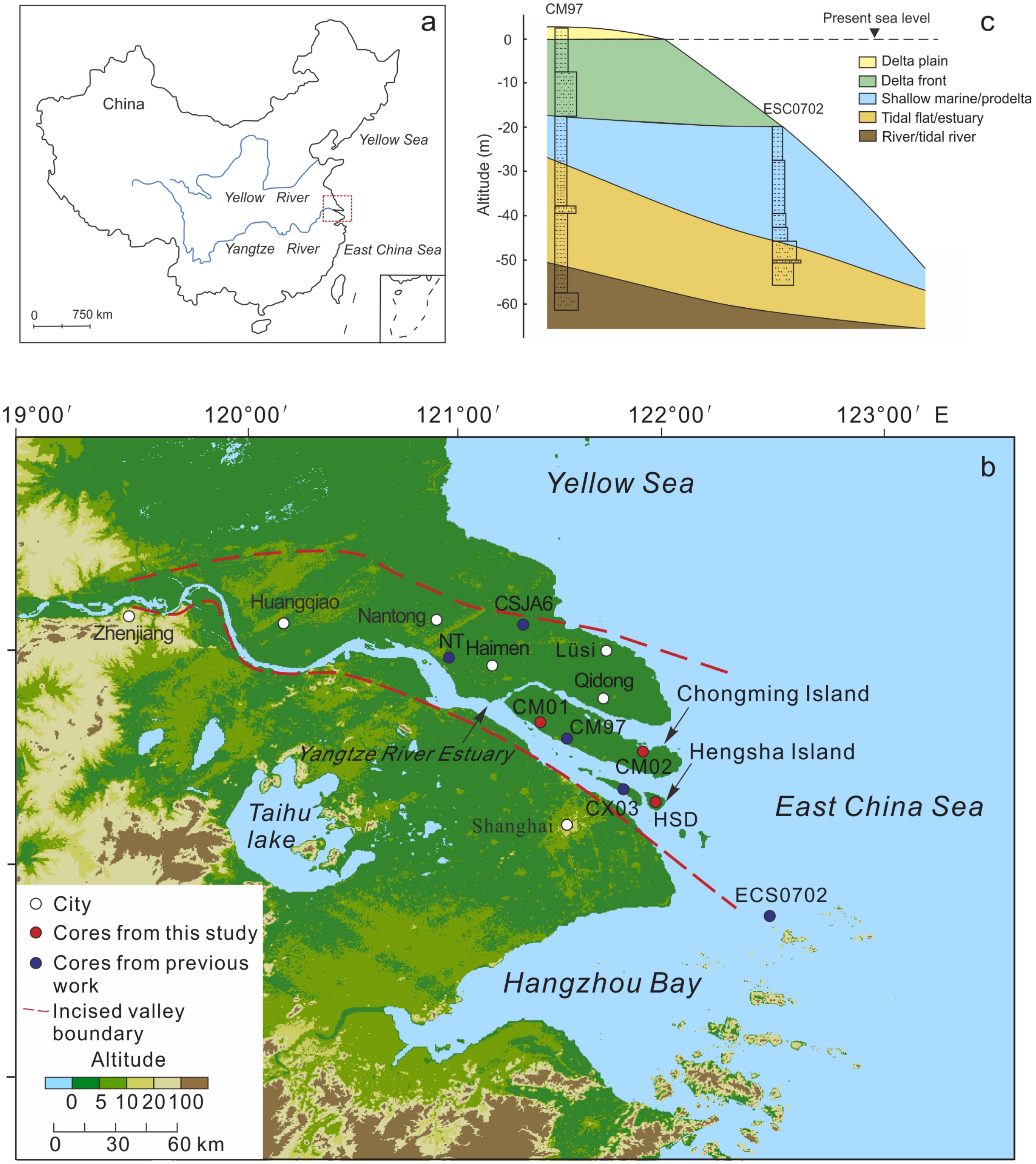
a
China
Yellow Sea
Yellow River
Yangtze River
East China Sea
0
750 km
c
CM97
Present sea level
ESC0702
0
-10
-20
-30
-40
-50
-60
Altitude (m)
Delta plain
Delta front
Shallow marine/prodelta
Tidal flat/estuary
River/tidal river
b
119°00′
120°00′
121°00′
122°00′
123°00′ E
32°00′
31°00′
30°00′
Yellow Sea
Zhenjiang
Huangqiao
Nantong
CSJA6
NT
Haimen
Lüsi
Qidong
Chongming Island
CM01
CM97
Hengsha Island
CM02
CX03
HSD
Yangtze River Estuary
Taihu lake
Shanghai
East China Sea
ECS0702
Hangzhou Bay
City
Cores from this study
Cores from previous work
Incised valley boundary
Altitude
0
5
10
20
100
0
30
60 km

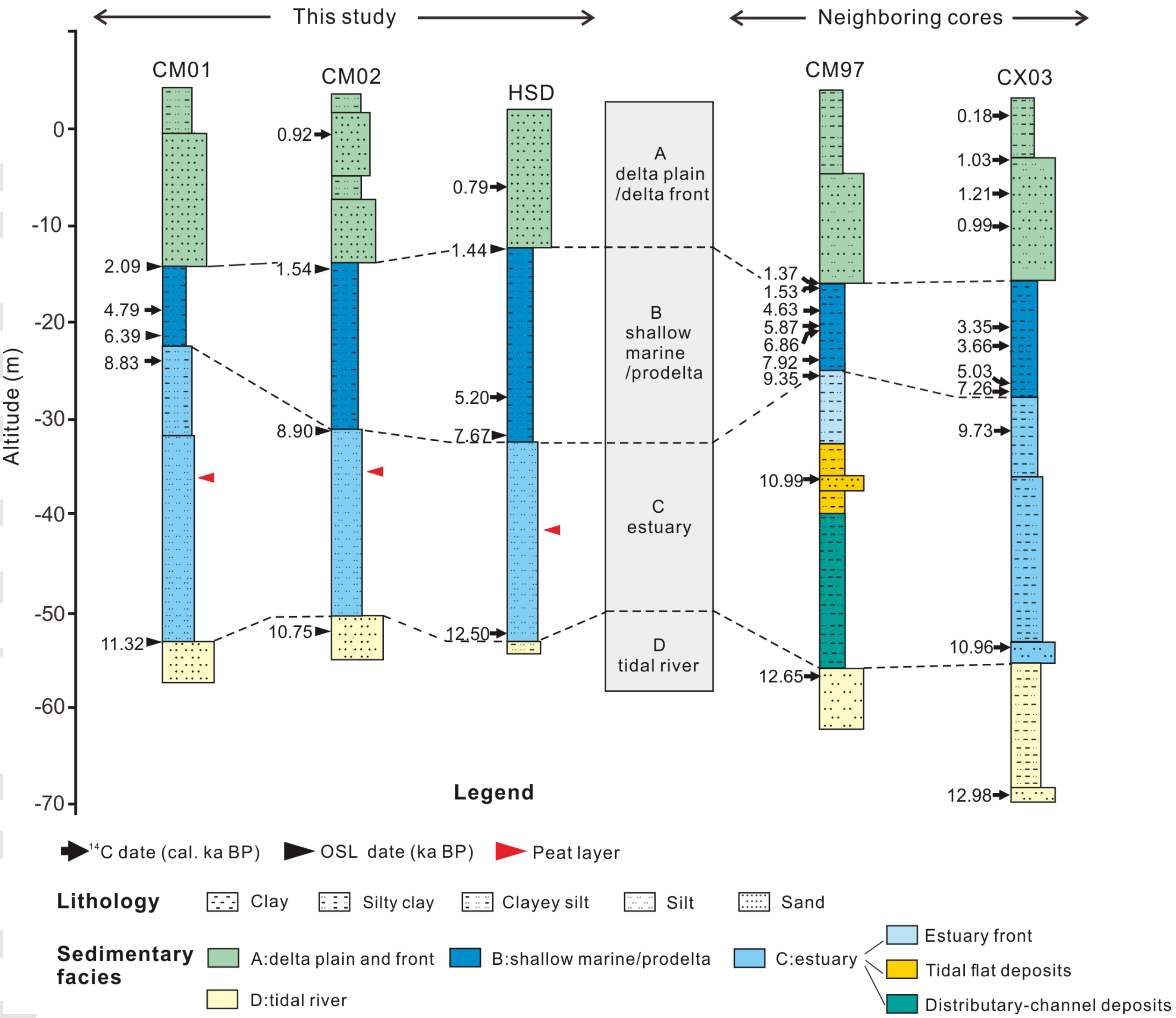
This study
Neighboring cores
CM01
CM02
HSD
CM97
CX03
Altitude (m)
0
-10
-20
-30
-40
-50
-60
-70
2.09
4.79
6.39
8.83
11.32
0.92
1.54
8.90
10.75
0.79
1.44
5.20
7.67
12.50
A
delta plain
/delta front
B
shallow
marine
/prodelta
C
estuary
D
tidal river
1.37
1.53
4.63
5.87
6.86
7.92
9.35
10.99
12.65
0.18
1.03
1.21
0.99
3.35
3.66
5.03
7.26
9.73
10.96
12.98
Legend
^{14}C date (cal. ka BP)
OSL date (ka BP)
Peat layer
Lithology
Clay
Silty clay
Clayey silt
Silt
Sand
Sedimentary facies
A:delta plain and front
B:shallow marine/prodelta
C:estuary
D:tidal river
Estuary front
Tidal flat deposits
Distributary-channel deposits

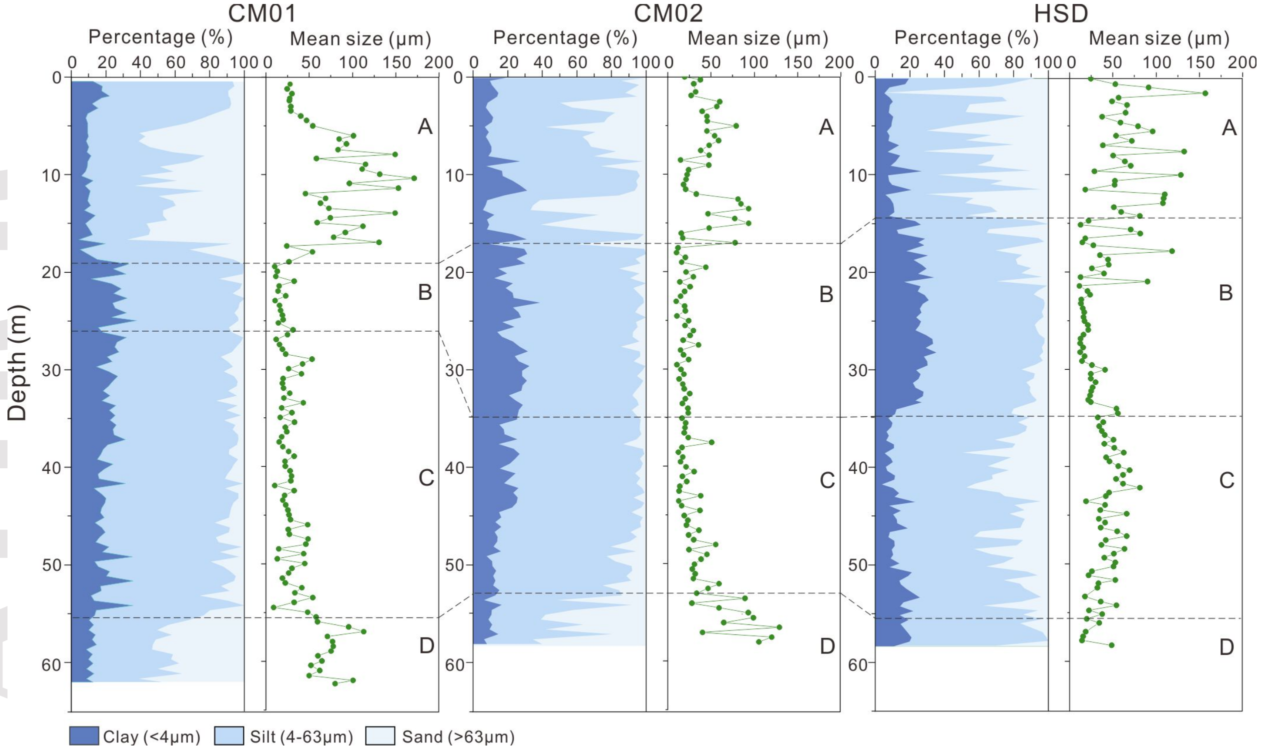
CM01
CM02
HSD
Percentage (%)
Mean size (μm)
0 20 40 60 80 100
0 50 100 150 200
Depth (m)
0
10
20
30
40
50
60
A
B
C
D
Clay (<4μm)
Silt (4-63μm)
Sand (>63μm)

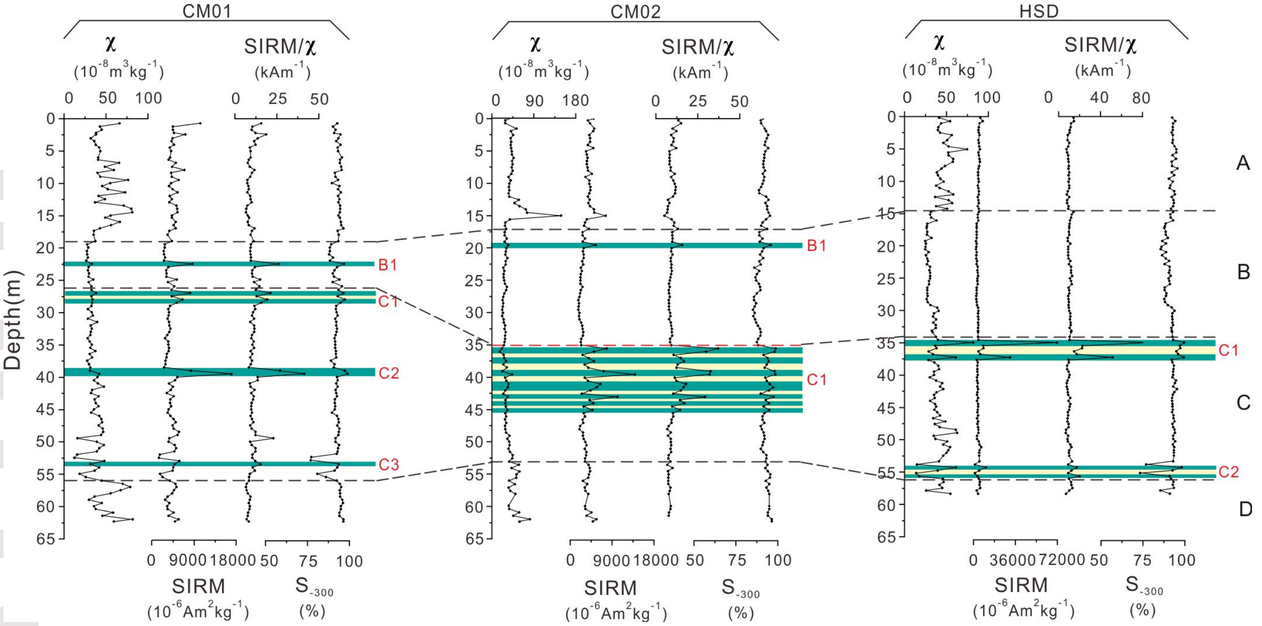
CM01
CM02
HSD
χ
(10^{-8}m^{3}kg^{-1})
SIRM/χ
(kAm^{-1})
SIRM
(10^{-6}Am^{2}kg^{-1})
S$_{-300}$
(%)
Depth(m)
0
5
10
15
20
25
30
35
40
45
50
55
60
65
0 50 100
0 25 50
0 9000 18000
50 75 100
0 90 180
0 36000 72000
0 40 80
B1
C1
C2
C3
A
B
C
D

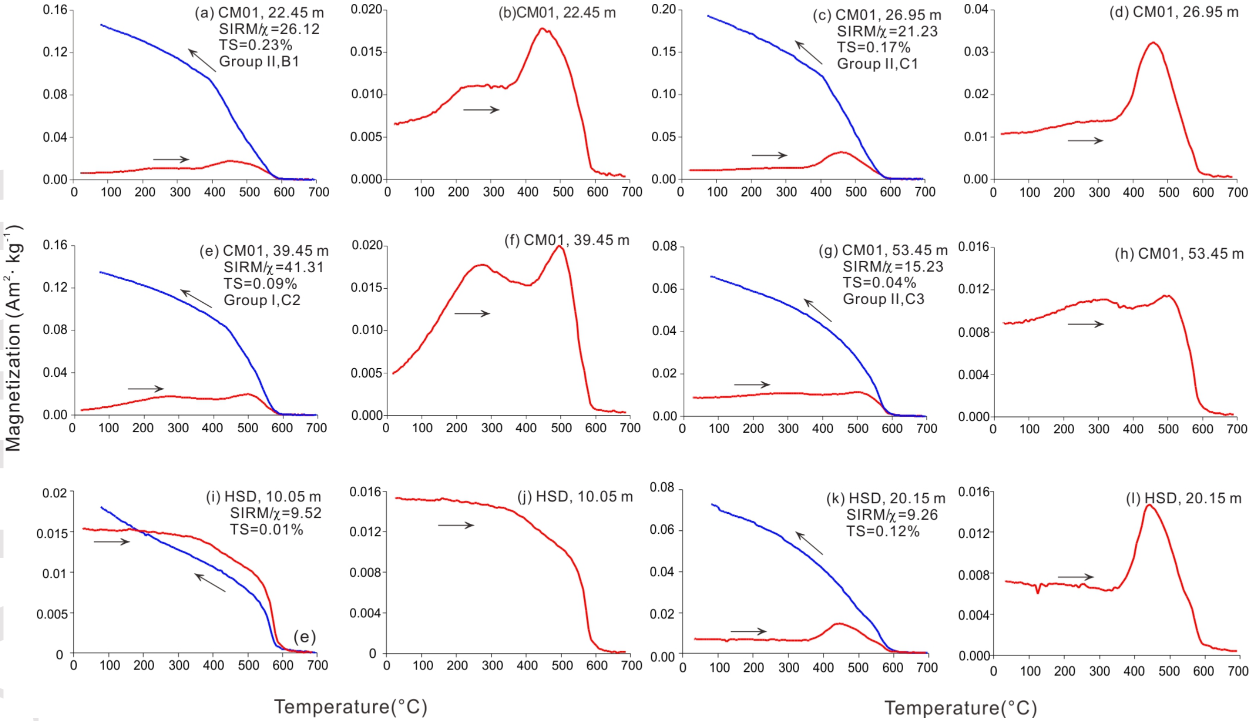
(a) CM01, 22.45 m
SIRM/χ=26.12
TS=0.23%
Group II,B1
(b)CM01, 22.45 m
(c) CM01, 26.95 m
SIRM/χ=21.23
TS=0.17%
Group II,C1
(d) CM01, 26.95 m
(e) CM01, 39.45 m
SIRM/χ=41.31
TS=0.09%
Group I,C2
(f) CM01, 39.45 m
(g) CM01, 53.45 m
SIRM/χ=15.23
TS=0.04%
Group II,C3
(h) CM01, 53.45 m
(i) HSD, 10.05 m
SIRM/χ=9.52
TS=0.01%
(e)
(j) HSD, 10.05 m
(k) HSD, 20.15 m
SIRM/χ=9.26
TS=0.12%
(l) HSD, 20.15 m
Magnetization (Am². kg⁻¹)
Temperature(°C)
Temperature(°C)
0 100 200 300 400 500 600 700

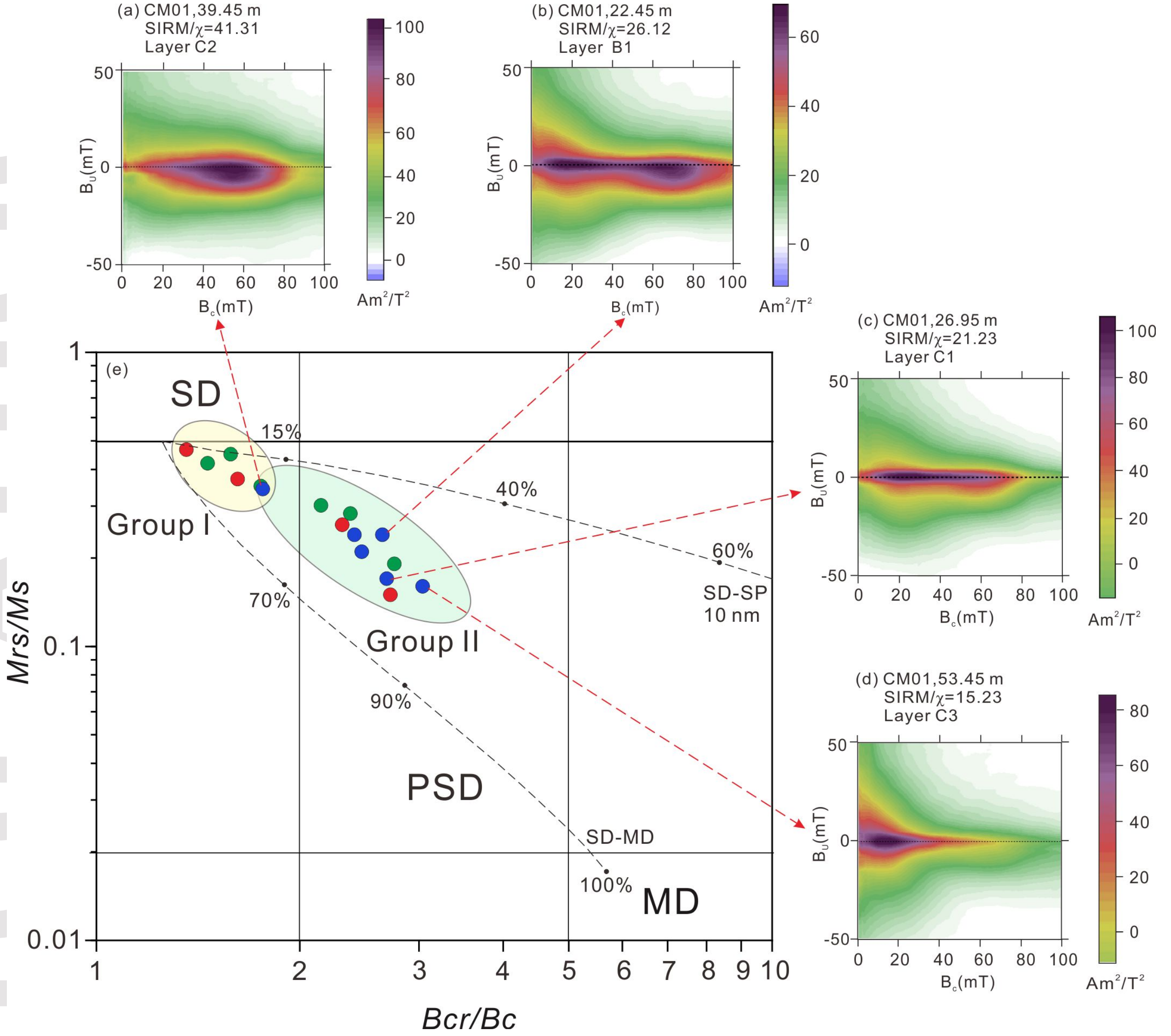
(a) CM01,39.45 m
SIRM/χ=41.31
Layer C2
(b) CM01,22.45 m
SIRM/χ=26.12
Layer B1
(c) CM01,26.95 m
SIRM/χ=21.23
Layer C1
(d) CM01,53.45 m
SIRM/χ=15.23
Layer C3
B_U(mT)
B_c(mT)
Am²/T²
(e)
SD
PSD
MD
Group I
Group II
15%
40%
60%
70%
90%
100%
SD-SP
10 nm
SD-MD
Mrs/Ms
Bcr/Bc
1
0.1
0.01

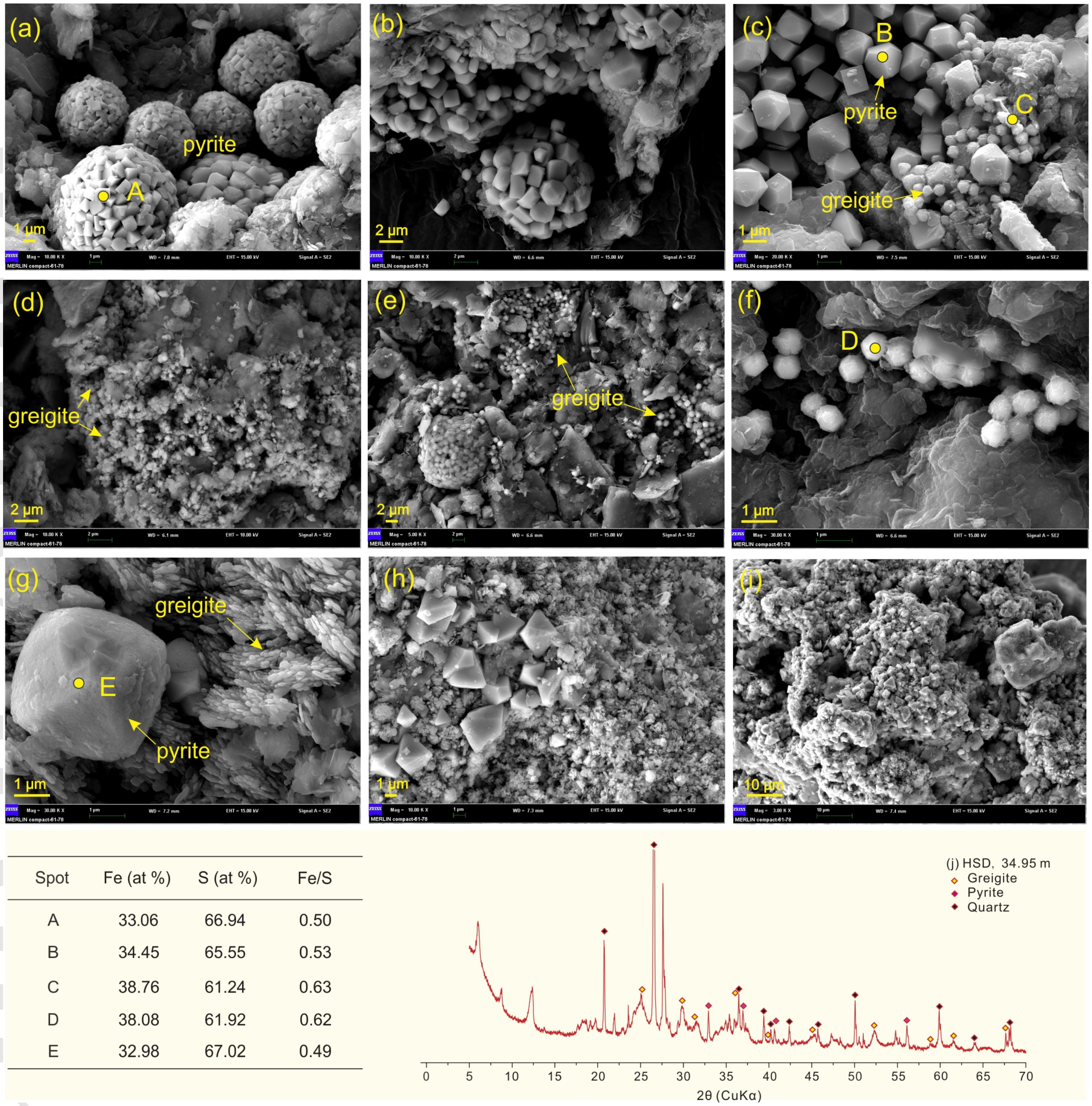

Spot	Fe (at %)	S (at %)	Fe/S
A	33.06	66.94	0.50
B	34.45	65.55	0.53
C	38.76	61.24	0.63
D	38.08	61.92	0.62
E	32.98	67.02	0.49

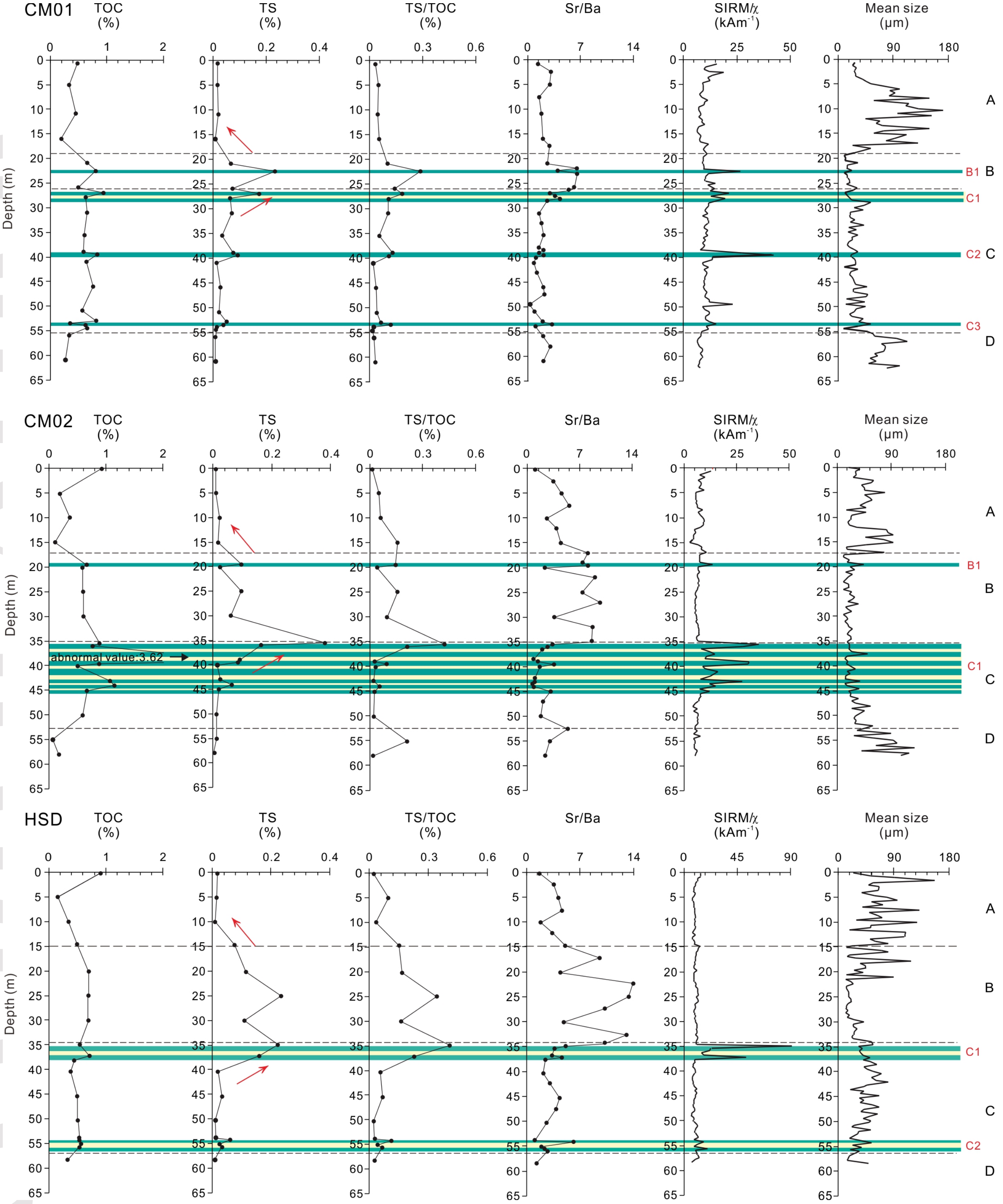
CM01
TOC (%)
TS (%)
TS/TOC (%)
Sr/Ba
SIRM/χ (kAm⁻¹)
Mean size (μm)
0 1 2
0 0.2 0.4
0 0.3 0.6
0 7 14
0 25 50
0 90 180
Depth (m)
0 5 10 15 20 25 30 35 40 45 50 55 60 65
A
B
C
D
B1
C1
C2
C3
CM02
abnormal value:3.62
HSD
0 45 90
C2

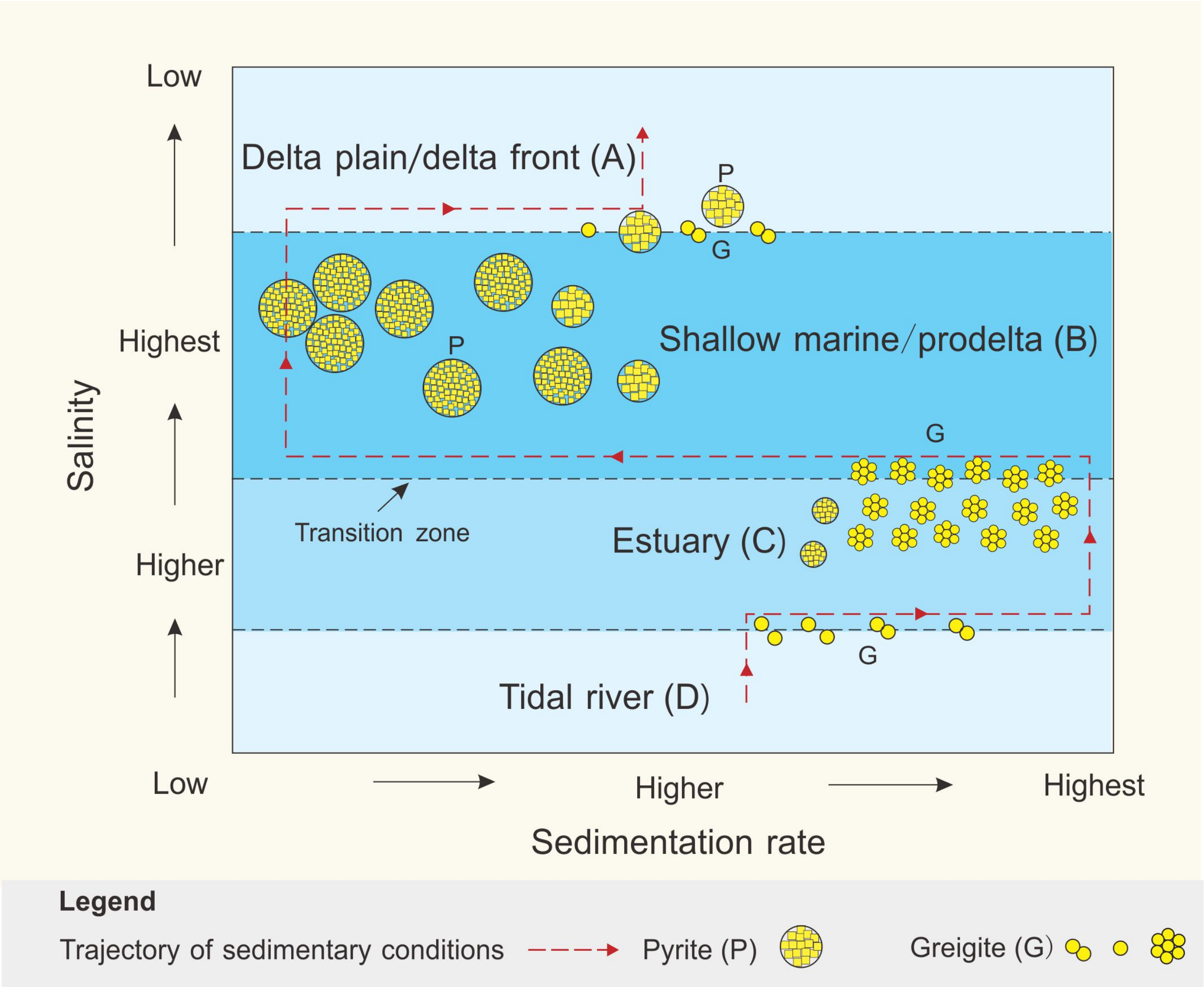
Low
Delta plain/delta front (A)
P
G
Highest
Shallow marine/prodelta (B)
P
Salinity
G
Transition zone
Higher
Estuary (C)
G
Tidal river (D)
Low
Higher
Highest
Sedimentation rate
Legend
Trajectory of sedimentary conditions
Pyrite (P)
Greigite (G)

Table 1. AMS ^{14}C ages for cores CM01, CM02 and HSD

Sample ID	Laboratory number	Depth (m)	Dating material	δ^{13}C (‰)	Conventional ^{14}C age		Calibrated ^{14}C age	ka BP
					a BP	error	(cal. a BP, 2σ)	
CM01-23	Beta-533819	22.73-22.74	shell	-1.0	4740	30	4613-4961	4.79 ± 0.17
CM01-29	Beta-533820	28.99-29.01	shell	-4.6	8460	30	8657-9011	8.83 ± 0.17
CM02-06	Beta-533821	4.49-4.52	shell	-3.8	1540	30	776-1066	0.92 ± 0.15
HSD-09	Beta-533822	7.69-7.70	shell	-5.3	1410	30	667-919	0.79 ± 0.13
HSD-33	Beta-533817	29.84-29.85	shell	-0.9	5060	30	5007-5383	5.20 ± 0.19
HSD-60	Beta-533818	53.38-53.40	shell	-6.8	11130	30	12335-12663	12.50 ± 0.16

Table 2. OSL ages for cores CM01, CM02 and HSD. The adopted ages are shown in bold and were selected following the statistical procedure of Arnold et al. (2007).

Core	Sample ID	Depth (m)	U (ppm)	Th (ppm)	K (%)	Water content (%)	Dose Rate (Gy/ka)	CAM-D$_e$ (Gy)	CAM-Age (ka)	MAM-D$_e$ (Gy)	MAM-Age (ka)
CM01	L505	17.79	1.62 ± 0.02	8.41 ± 0.12	1.62 ± 0.02	25 ± 10	2.21 ± 0.15	4.78 ± 0.12	2.09 ± 0.15	**4.78 ± 0.24**	**2.09 ± 0.18**
CM01	L514	25.85	2.01 ± 0.03	10.92 ± 0.20	1.90 ± 0.01	33 ± 10	2.51 ± 0.16	18.91 ± 0.63	7.48 ± 0.54	**16.18 ± 1.07**	**6.39 ± 0.59**
CM01	L542	54.05	2.10 ± 0.01	11.19 ± 0.11	1.93 ± 0.01	25 ± 10	2.73 ± 0.19	**31.12 ± 0.63**	**11.32 ± 0.81**	31.16 ± 1.14	11.34 ± 0.88
CM02	L572	17.70	1.96 ± 0.01	12.32 ± 0.27	2.41 ± 0.03	43 ± 10	2.72 ± 0.16	4.37 ± 0.06	1.54 ± 0.10	**4.38 ± 0.08**	**1.54 ± 0.10**
CM02	L590	35.70	2.00 ± 0.02	10.70 ± 0.10	2.00 ± 0.01	31 ± 10	2.59 ± 0.17	**23.20 ± 0.53**	**8.90 ± 0.61**	23.20 ± 1.15	8.90 ± 0.76
CM02	L611	56.57	1.21 ± 0.03	6.08 ± 0.05	1.62 ± 0.01	26 ± 10	1.93 ± 0.13	**20.91 ± 0.64**	**10.75 ± 0.82**	18.26 ± 1.23	9.38 ± 0.73
HSD	L437	15.35	1.87 ± 0.01	11.15 ± 0.09	1.81 ± 0.01	37 ± 10	2.37 ± 0.14	3.63 ± 0.11	1.46 ± 0.10	**3.56 ± 0.20**	**1.44 ± 0.12**
HSD	L458	33.95	2.42 ± 0.12	13.40 ± 0.67	2.14 ± 0.11	36 ± 10	2.81 ± 0.19	22.01 ± 0.45	7.76 ± 0.54	**21.78 ± 0.95**	**7.67 ± 0.62**

[a] D$_e$ = Equivalent dose: laboratory dose of beta or gamma radiation needed to induce luminescence equal to that acquired by a sample subsequent to the most recent bleaching event (usually taken to be coincident with deposition). Unit: gray (Gy); Dose Rate = Dose per unit of time received by the sample while buried Unit: Gy/ka (Aitken, 1998).

[b] CAM = central age model; MAM = minimum age model (Galbraith et al., 1999).

[c] “ka” in the table is relative to 1950 AD for comparision to AMS ^{14}C ages.